ELSEVIER

Contents lists available at ScienceDirect

# Sensors and Actuators B: Chemical

journal homepage: www.elsevier.com/locate/snb



# Photonic crystal-enhanced fluorescence imaging immunoassay for cardiovascular disease biomarker screening with machine learning analysis



Kenneth J. Squire<sup>a</sup>, Yong Zhao<sup>a,b</sup>, Ailing Tan<sup>a,c</sup>, Kundan Sivashanmugan<sup>a</sup>, Joseph A. Kraai<sup>d</sup>, Gregory L. Rorrer<sup>d</sup>, Alan X. Wang<sup>a,\*</sup>

- a School of Electrical Engineering and Computer Science, Oregon State University, 1148 Kelley Engineering Center, Corvallis, OR, 97331, USA
- <sup>b</sup> School of Electrical Engineering, The Key Laboratory of Measurement Technology and Instrumentation of Hebei Province, Yanshan University, Qinhuangdao, Hebei, 066004, PR China
- <sup>c</sup> School of Information Science and Engineering, The Key Laboratory for Special Fiber and Fiber Sensor of Hebei Province, Yanshan University, Qinhuangdao, Hebei, 066004. PR China
- d School of Chemical, Biological & Environmental Engineering, Oregon State University, 116 Johnson Hall, Corvallis, OR, 97331, USA

#### ARTICLE INFO

#### Keywords: Fluorescence imaging Photonic crystals Immunoassay Cardiovascular biomarker Machine learning

#### ABSTRACT

When myocardial walls experience stress due to cardiovascular diseases, like heart failure, hormone N-terminal pro-B-type natriuretic peptide (NT-proBNP) is secreted into the blood. Early detection of NT-proBNP can assist diagnosis of heart failure and enable early medical intervention. A simple, cost-effective detection technique such as the widely used fluorescence imaging immunoassay is yet to be developed to detect clinically relevant levels of NT-proBNP. In this work, we demonstrate photonic crystal-enhanced fluorescence imaging immunoassay using diatom biosilica, which is capable of detecting low levels of NT-proBNP in solution with the concentration range of 0~100 pg/mL. By analyzing the fluorescence images in the spatial and spatial frequency domain with principle component analysis (PCA) and partial least squares regression (PLSR) algorithms, we create a predictive model that achieves great linearity with a validation R<sup>2</sup> value of 0.86 and a predictive root mean square error of 14.47, allowing for good analyte quantification. To demonstrate the potential of the fluorescence immunoassay biosensor for clinical usage, we conducted qualitative screening of high and low concentrations of NT-proBNP in human plasma. A more advanced machine learning algorithm, the support vector machine classification, was paired with the PCA and trained by 160 fluorescence images. In the 40 testing images, we achieved excellent specificity of 93%, as well as decent accuracy and sensitivity of 78% and 65% respectively. Therefore, the photonic crystal-enhanced fluorescence imaging immunoassay reported in this article is feasible to screen clinically relevant levels of NT-proBNP in body fluid and evaluate the risk of heart failure.

## 1. Introduction

According to the American Heart Association, in 2009, one in nine deaths cited heart failure (HF) as a contributing cause and in 2016, about 5.7 million Americans suffered from HF [1]. Total direct medical costs of HF in the US are projected to be \$42.9 billion by 2020 [2]. The need for accurate, inexpensive and early detection of HF is of critical importance. When an individual has HF, the myocardial wall experiences stress and the prohormone B-type natriuretic peptide (proBNP) is cleaved releasing N-terminal proBNP (NT-proBNP) and BNP. Both are recommended by the European Society of Cardiology (ESC) as analytes to aid in the diagnosis of HF [3]. However, the half-life-time of NT-proBNP is nearly  $6 \times 10^{-10}$  longer than that of BNP, making it a better

biomarker for detection [4]. The ESC directs that the upper limit of normal levels of the biomarker is 125 pg/mL and values lower than this can be used to rule out the possibility of HF [3]. Levels of NT-proBNP > 450 pg/mL can be used to "rule in" HF [5].

The most common method of detecting NT-proBNP is by performing electrochemiluminescence (ECL) paired with an immunoassay. This method is recommended and used by respected institutions such as the Mayo Clinic [6,7]. ECL is effective, but it also requires expensive, sophisticated instrumentation and highly trained personnel. Fluorescence imaging, often paired with an immunoassay, is a biosensing technique that could be used in place of ECL. The immunoassay allows for high degrees of specificity due to the specific antibody-antigen interaction, allowing capture or separation of the analyte from the surrounding

E-mail address: wang@oregonstate.edu (A.X. Wang).

<sup>\*</sup> Corresponding author.

sample matrix. Fluorescence imaging sensors are rationally designed such that the presence of the analyte induces a change in fluorescence intensity, which is caused by specific analyte labeling with a fluor-ophore [8–10]) or quenching inherent sample fluorescence [11,12].

Fluorescence imaging employs imagers, either consumer or laboratory grade, to monitor the change in fluorescence intensity. The intensity depends on the concentration of analyte present, and in some applications, detection and quantification can be achieved even down to single molecule levels [13,14]. Furthermore, fluorescence imaging can perform large area measurements while maintaining spatial information, thus allowing parallel sensing of multiple sensors for highthroughput applications. This powerful sensing technique has been applied to the detection of NT-proBNP [15,16]. However, Lee et al. [15] achieved detection of the biomarker only to 5 ng/mL, which is significantly above clinically relevant levels. Wilkins et al. [16] successfully detected NT-proBNP down to 50 pg/mL but required high efficiency quantum dots containing toxic cadmium sulfide to achieve this level of detection. Therefore, safe detection of NT-proBNP at clinically relevant levels of detection still requires further fluorescence signal enhancement.

In recent years, plasmonic structures such as nanoparticles, nanorods and other nanostructures have been employed to enhance the local electromagnetic field resulting in enhanced fluorophore excitation [17–19]. These techniques provide fluorescence enhancement but often suffer highly localized effects. Uniform photonic crystals have also been used as suitable fluorescence enhancing substrates due to their optical field enhancement and large sensing area-to-volume ratio [20–23]. However, rationally designed photonic crystals generally require cleanroom technologies to fabricate and often experience issues with surface functionalization [24,25]. Engineered fluorophores, such as quantum dots, have been fabricated and used to achieve higher quantum efficiencies and stronger fluorescence, but these often require toxic materials such as cadmium [26,27].

Other than the concern of sensitivity, random fluctuation of the fluorescence signals brings a great challenge for analyte quantization. Feature extraction, statistical regressions and classifications are the main tasks of statistical machine learning with each algorithm being used to improve the clarity of a dataset for quantitative and qualitative analyses. Feature extraction techniques, such as principle component analysis (PCA), reduce the dimensionality of data, enabling more effective visualization and analysis. Regression analyses, like the partial least squares regression (PLSR) or support vector regression, are common analytical techniques that have been applied to fluorescence biosensing and allow for the creation of accurate calibration curves to quantitatively predict the concentration of an analyte [28-30]. Classification techniques such as the linear discriminant analysis, k-nearest neighbors (kNN) or support vector machines (SVM) can be used to train a model capable of accurately grouping data points by similar characteristics and are effective for qualitative and semi-quantitative classification. Implementation of classification techniques have enabled successful analyte detection with fluorescence biosensing [31–33].

In this work, we demonstrated a photonic crystal-enhanced fluorescence imaging immunoassay biosensor capable of detecting clinically relevant levels of NT-proBNP and implemented machine learning-assisted analyte quantization. Different than artificial photonic crystals made by top-down nanofabrication techniques, our cardiovascular biomarker sensor employs diatom biosilica to enhance the fluorescence signal. Diatoms are single-celled microalgae that biologically fabricate porous silica shells called frustules. The periodic, nanostructured pore arrays of diatom frustules can enable natural photonic crystal behavior. Our group has proven that diatom biosilica is capable of enhancing Raman and fluorescence signals due to their photonic crystal structure as well as their large and super-hydrophilic surface, thus offering exclusive advantages for biosensing, particularly for immunoassay [34–37]. The biosensor fabrication begins with cost-effective algae cultivation to grow diatoms. Cellular organic matter is removed, and

the isolated biosilica shells are deposited onto a glass slide as a dispersed monolayer thin film. A typical sandwich immunoassay process is performed to functionalize the substrate with antibodies, selectively capturing the analyte NT-proBNP and tagged with fluorophore-labeled antibodies. The diatom biosilica integrated with our sensor offers significant fluorescence signal enhancement for clear imaging. Following the data acquisition, a simple arithmetic average fluorescence intensity analysis is performed, resulting in the detection of NT-proBNP to clinically relevant levels but with difficulty in differentiation at lower concentrations. To improve this, feature extraction and regression analyses obtain an excellent calibration curve for the NT-proBNP concentration with good linearity and differentiation. When challenged by 24 test images, a validation R<sup>2</sup> value of 0.86 and a predictive root mean square error of 14.47 was achieved, allowing for good analyte quantification. Lastly, we detect NT-proBNP in human plasma and use feature extraction and classification to qualitatively distinguish between high and low concentrations of NT-proBNP, creating a screening mechanism for diagnostically ruling in or out heart failure. The classification model was trained using 160 fluorescence images and when applied to 40 test images, achieves excellent specificity of 93%, and decent accuracy and sensitivity of 78% and 65% respectively. Therefore, the synergistic integration of the photonic crystal-enhanced fluorescence imaging immunoassay with machine-learning analysis techniques has led to effective detection of cardiovascular biomarker NT-proBNP, which can play a key role for screening individuals with heart failure risk.

#### 2. Materials and methods

#### 2.1. Diatom-based NT-proBNP sensor fabrication

The fabrication follows our earlier work with minor modifications [37]. Diatom culturing and isolation techniques as well as populating a coverslip are described in the Supporting Information. Scanning electron microscopy (SEM) images of the coverslips are shown in Fig. 1(a and b) and discussed in the Supporting Information. The process of the sandwich type immunoassay is outlined in the schematic in Fig. 1(c) below

Briefly, a  $2.2 \times 2.2 \, \text{cm}$  glass coverslip with diatom frustule mass coverage of 5 µg/cm<sup>2</sup> was first submerged in a mixture of 10 mL methanol, 500 µL of 99% acetic acid and 150 µL of 99% (3-Aminopropyl)triethoxysilane (APTES) for 30 min at room temperature to populate the surface with free amine groups. The sample was rinsed with acetone and ethanol and dried with nitrogen. The sample was then submerged in 2% glutaraldehyde (GA), a homobifunctional crosslinker, in phosphate buffered saline (PBS) for 2 h at room temperature to react with the free amine group and to cover the surface with aldehyde groups. Following a rinsing with 20 mM 4-(2-hydroxyethyl)-1-piperazineethanesulfonic acid (HEPES) and deionized water, the glass coverslip was dried with nitrogen gas flow and diced into multiple  $5\times 5\,\text{mm}$  sensors. Each sensor then had  $1\,\mu\text{L}$  of  $0.1\,\text{mg/mL}$  of the antibody, anti-proBNP, dropcast onto its surface. It was left at 4 °C for 6 h to allow the surface to be functionalized with the antibody. The sample was again rinsed with HEPES and water and dried with nitrogen gas. Next, the sample was submerged in 1 mg/mL bovine serum albumin (BSA) in PBS for 6 h at 4 °C to block all the remaining aldehyde groups. This decreases nonspecific binding and enhances the detection specificity of the immunoassay sensor. Again, the sample was rinsed with HEPES and water, and dried by nitrogen gas. At this point, the functionalized immunoassay sensor was ready for detection. The detection was performed by submerging the sample in a solution of NT-proBNP analyte in either PBS or human plasma. This step was performed in solution volumes of 900 mL and 400 µL for the buffer and plasma respectively. The sensor was kept in the solution for 2h at room temperature to allow for immune-recognition of the antibody-antigen pair. After another rinsing with HEPES and water, the sample had  $1\,\mu L$  of 0.25 mg/mL anti-NT-proBNP conjugated with fluorescein dropcast onto

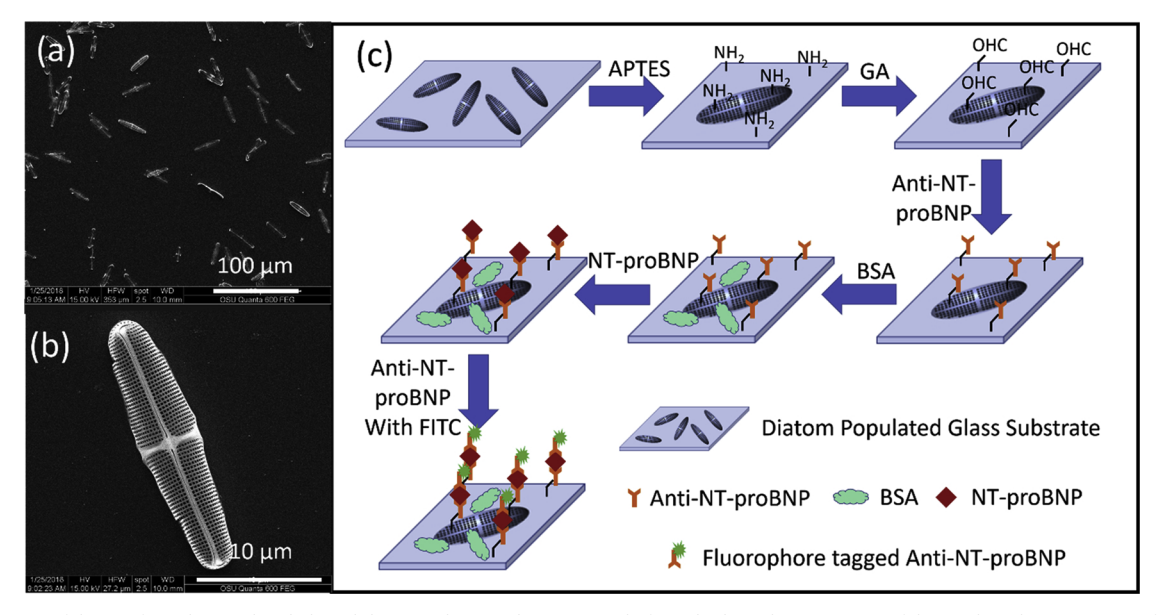


Fig. 1. SEM image of diatom frustule-populated glass slide (a) and zoomed in on a single frustule (b). Schematic view of diatom-based immunoassay for NT-proBNP detection (c).

the surface, where it was left for 4 h at 4 °C, thus labeling the bound antigens with fluorophore labeled antibodies and completing the immune-sensing process.

#### 2.2. Fluorescence image preprocessing and processing

The details about the fluorescence microscope, light source, and image capture parameters are described in the Supporting Information. The acquired optical and fluorescence images were saved as. tiff files and imported into Matlab to be prepared for processing, following the similar approach outlined in our previous work [37], which is described in Fig. 2. Optical and fluorescence images were first superimposed on top of one another and aligned. Frustules in the image were then circled and a mask was created in the shape of the diatom shell. This mask was applied to the original fluorescence image, leaving just the frustule with

the remainder of the background zeroed out. Once the fluorescence image was masked, it was cropped to a uniform size with the frustule in the center. Another set of images were constructed from the original image with the frustules zeroed, leaving only the fluorescence information on glass. These spatial domain images were used to analyze the fluorescence signal on glass and compare it to that found on diatom frustule.

After the diatom frustules from the fluorescence image were masked and cropped, the power spectral density (PSD) of each image was obtained by performing the two-dimensional fast Fourier transform (FFT) and taking the square of the absolute value in the spatial frequency domain. The image was shifted to move the zero-frequency component to the middle of the image and the natural log-scale was taken.

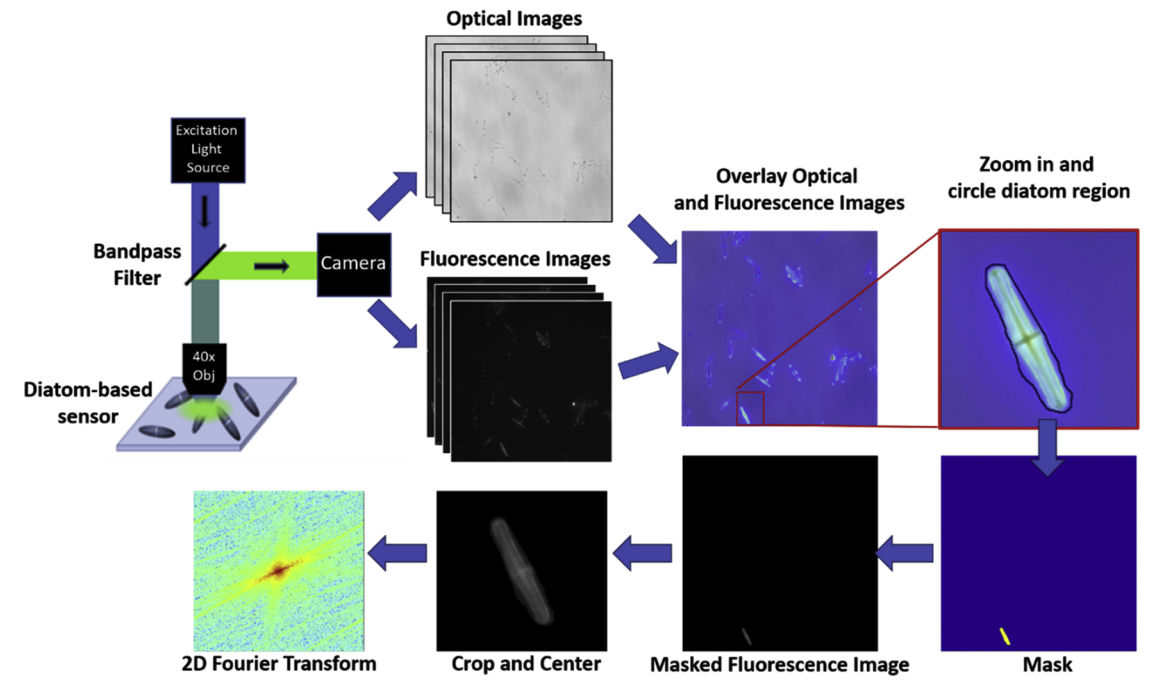


Fig. 2. Schematic view of the preprocessing applied to the fluorescence images to prepare the images to be analyzed.

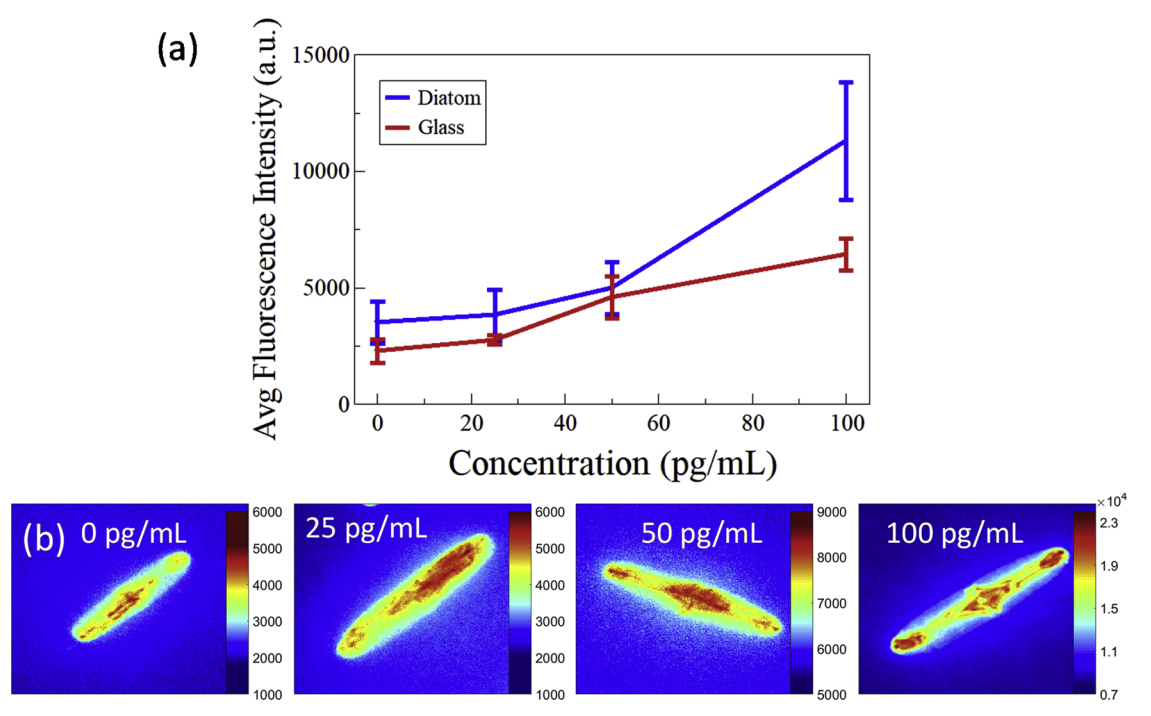


Fig. 3. A comparison plot of average fluorescence intensity on diatom biosilica and glass (a). Representative fluorescence images of the frustules (b).

#### 2.3. Statistical regression calibration curve creation

To create the calibration curve for solution-based NT-proBNP sensing, PCA was paired with PLSR. The model was created by first, using Matlab to find the average fluorescence intensity for each concentration by finding the average intensity of each PSD of the frequency domain image and taking the total average. Once the average intensity for each concentration was determined, 30 images with average intensities closest to the concentration's average fluorescence intensity were selected. This was done for each concentration to remove any outliers and resulted in a dataset of 30 images from each concentration. Using the built-in Matlab functions, the principle components (PCs) were determined and the first three were used in PLSR. A 5-fold cross-validation was used where 80% of the images were used to train a model and 20% were used to test the model.

From the training and test regressions, the coefficient of determination ( $R^2$ ) and the root mean square error (RMSE) were calculated from the 5-fold cross-validations and were averaged. The equations for these values are shown in the Supporting Information. The RMSE is a measure of the average error predicted within the dataset and explains how spread out the data is and the  $R^2$  is a measure of how good of a fit the regression gives. Generally, higher  $R^2$  (but no more than 1) and lower RMSE values means better regression performance. Discussion of our created model is given in Section 3.3.

#### 2.4. Qualitative screening procedure

To perform the qualitative screening of NT-proBNP in human plasma, the data preparation was similar to that of the regression analysis but 100 frequency domain images at high and low concentrations were chosen instead of 30 due to our larger plasma-based measurements dataset. PCA was performed on the images and classification algorithms including kNN and SVM were used in this analysis. kNN was achieved using Matlab's built-in function and SVM classification was performed using a common SVM library, libSVM [38]. The accuracy, sensitivity and specificity for each classification algorithm were calculated for various numbers of PCs using a 5-fold cross-validation and the average of each statistic were compared and discussed in

Section 3.4 below. These metrics are defined thoroughly in our Supporting Information. Briefly, the model classifies the dataset into a positive and negative class, which correspond to the high concentration and low concentration, respectively. Accuracy is a measure of how many measurements the model correctly classified. Sensitivity is a measure of the number of correctly classified positive measurements, and specificity describes the number of correctly classified negative measurements. Each of these metrics range from 0 to 1 with 1 being perfect classification.

## 3. Results and discussion

## 3.1. Cardiovascular disease biosensing mechanism

The sandwich immunoassay process used here is one that is fairly well understood and accepted. The diatom-populated glass slide is first aminated using the APTES, resulting in free amine groups on its surface. The homobifunctional crosslinker GA is then introduced. This molecule contains two aldehyde groups, one of which easily reacts with the free amine group, leaving the other free, thus populating the surface with free aldehyde groups. These aldehydes easily react with amine groups on the antibody, anti-NT-proBNP, and the protein BSA. The substrate is populated with capture antibodies, after which, BSA is used to block the remaining active aldehydes to reduce nonspecific binding. The analyte is then introduced and selectively binds with the capture antibody affixed to the substrate through immunorecognition. Lastly, antibodies labeled with a fluorescent tag (anti-NT-proBNP-FITC) are introduced, where they bind with the antigen and complete the sandwich structure. At this point, the sensing event has taken place and the fluorescence can now be measured. The characterization of this substrate is discussed in more depth in the Supporting Information.

## 3.2. Average intensity analysis

To analyze the efficacy of our diatom-based fluorescence NT-proBNP biosensor, the immunoassay, image collection and preprocessing of the fluorescence images were performed as explained in Sections 2.1 and 2.2 above, followed by an average intensity analysis. To begin,

the average fluorescence intensity of each spatial domain image was calculated for a given concentration. The median average intensity was found, and images with an average fluorescence intensity greater than one standard deviation away from the median were excluded as outliers. The average and standard deviation of the remaining images' average fluorescence intensities were calculated for each concentration using the preprocessed spatial domain images of diatom frustules as well as the glass images. The results were plotted versus the analyte concentration as shown in Fig. 3(a). Fig. 3(b) shows the representative fluorescence images at those concentrations, which clearly highlights the enhanced fluorescence emission from the diatom biosilica due to the photonic crystal effect and surface effect. As can be seen in the figures, the fluorescence intensity on frustule is at least  $2 \times \text{higher}$  than that on glass and validates the use of frustules for enhancing the fluorophore's signals.

Description of the fluorescence enhancing mechanism of frustules is explained in the Supporting Information. Using this average fluorescence analysis, NT-proBNP concentration of 100 pg/mL is distinct since the signal is clearly above the error bar of the negative test (zero analyte concentration). However, for lower concentrations of analyte testing, the fluorescence signals are comparable to the error bar of the negative test, making it difficult to differentiate. A more sophisticated method of analysis is required to achieve better sensitivity and quantization.

#### 3.3. Quantitative statistical regression

While the average intensity analysis is simple and straightforward, the calibration curve is nonlinear with large variation, either with or without diatom frustules, resulting in a high limit of detection. Random errors during the immunoassay process and the statistical nature of fluorescence emission are the main causes of the error bars, which are intrinsic to the fluorescence imaging immunoassay. More advanced statistical analytical methods must be employed to improve the sensing performance.

Statistical regressions were performed using spatial domain images as well as the PSD of the spatial frequency domain images of preprocessed diatom images. Fig. 4(a) shows the spatial frequency domain images from the preprocessed diatom images. The central peak relates

to the zero-frequency component of the zeroed-out background and the points in the image further from the center represent higher frequency components of the diatom fluorescence image. The spike lines radiating from the center represent fluorescence signals in the spatial domain corresponding to the geometric feature of diatom frustules. For example, the minor axis of the diatom in the spatial domain is represented by the prominent line radiating from the center of the spatial frequency domain image along the same axis.

The aim of the regression is to correlate the fluorescence intensity and the analyte concentration. Optimal results were achieved by implementing PCA feature extraction with PLSR. Comparing the regression results applied to the spatial and spatial frequency domain images, spatial frequency domain images gave superior results and were thus used in this analysis. This may be due to the fact that the intensity variation among different concentrations in the spatial domain is slight, as seen in Fig. 3(a). However, the spatial frequency domain is a more detailed image space and is heavily influenced by changes in the spatial domain. The slight change in fluorescence intensity in the spatial domain results in a much greater change in the spatial frequency domain. PCA and PLSR rely on variation to differentiate analyte concentrations and thus the greater change in the spatial frequency domain allows for greater sensitivity of PCA and PLSR.

The number of PCs to include in the regression step affects the quality of the model achieved. We swept the number of components to include and compared their R2 values. This analysis is shown in our Supporting Information. Optimal results were achieved using the first three PCs and the training data are plotted in Fig. 4(b). The PLSR algorithm creates a model which can then be applied to a test set. As explained in Section 2.3, a 5-fold cross-validation was performed by training a model using 80% of the images and testing that model on the remaining 20% images. This allows verification of the utility of our model for future quantification. The calculated calibration curve from the training set was applied to the test dataset. The calibration fit, as well as that obtained when validating the model, are shown in Fig. 4(c) below. Applying this model to the test dataset, we achieved good linearity with a R2 testing value of 0.86 and a predicted RMSE (RMSEP) of 14.47. The high R<sup>2</sup> value and the low RMSEP indicate accurate quantifications of NT-proBNP detection down to 19 pg/mL.

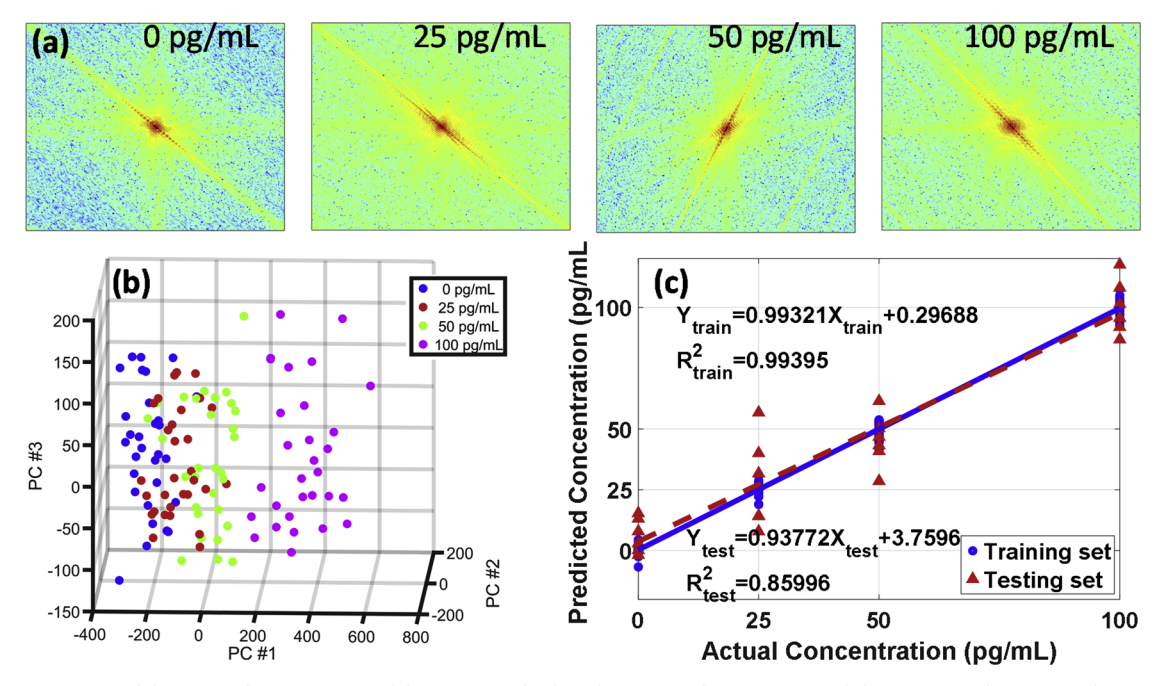


Fig. 4. Representative spatial frequency domain images of diatoms (a). The first three principle components of the images in the training dataset (b). Predictive model achieved using optimized statistical regression parameters on the training dataset, and the prediction results by applying the model to the testing dataset (c).

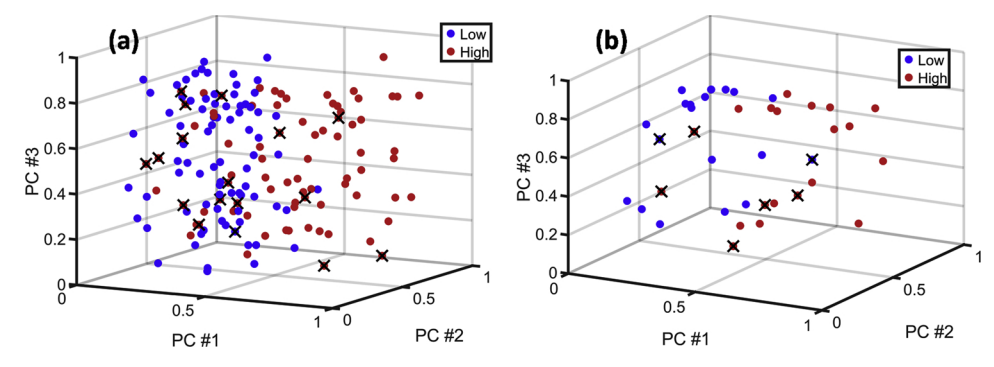


Fig. 5. Classification results of training (a) and test dataset (b) plotted with respect to the first three principle components extracted using PCA. The X's represent measurements that were incorrectly classified.

#### 3.4. Qualitative classification of NT-proBNP in plasma

In real-world applications, the detection of NT-proBNP is performed in a real biological fluid with competing biomolecules like proteins that can obscure the signal. To prove the validity of our photonic crystalenhanced fluorescence imaging immunoassay for future clinical usage, we performed the detection of NT-proBNP in human plasma. A qualitative classification screening was performed to determine the clinically relevant level of high or low concentration of NT-proBNP. According to the literature [3,5], if the NT-proBNP concentration is below 125 pg/ mL, it can be used to "rule out" heart failure. If the concentration is above 450 pg/mL, it can be used to "rule in" heart failure. For this classification, we combined measurements made at 10 and 50 pg/mL to be considered a low concentration class and measurements made at 500 pg/mL was a high concentration class. To ensure the same number of measurements were in each category, 50 images, with average intensities closest to the mean average intensity, were selected from each lower concentration. From the higher concentration, 100 measurements were taken, again, with average intensities closest to the total average intensity at this concentration.

The classification analysis was performed using PCA feature extraction combined with two classification techniques which were compared to find the best solution. The kNN and SVM are classification techniques that have been applied to both fluorescence imaging and spectroscopy biosensing [31–33]. kNN is a non-parametric classification method. An unlabeled test sample is classified by a majority vote of its k-nearest neighbors and the most frequent label is assigned to the class of the output. SVM algorithm is a widely used supervised learning method which can efficiently perform a non-linear classification using the nonlinear kernel function and fitting the maximum-margin hyperplane in a transformed feature space.

The two classification algorithms were applied after PCA of the spatial frequency domain images and parameters were swept to find the optimal solution for each algorithm. A 5-fold cross-validation was again performed to enable training of the model and testing. The parameters for SVM were optimized and the results are shown in Fig. 5(a) is the classification results from the training dataset and (b) is from the test dataset. Both are plotted with respect to the first three PCs. The color of each data point represents its actual concentration class and each point with an "X" represents measurements that were incorrectly classified.

From these classifications, the accuracy, sensitivity, and specificity

were calculated as explained in Section 2.4 above. These are common metrics that indicate the quality of the classification model where the closer to 1 (but less than 1), the better the classification model. The calculated metrics for the optimal solution for each classification technique were obtained from each of the five cross-validations. The metric averages and standard deviations are displayed in Table 1 and the two classification methods were compared. It was found that using SVM with enough PCs to account for 55% of the sample variation gave the best results.

As can be seen above, the SVM model has a predictive accuracy and sensitivity that are slightly lower than desired. However, the specificity, of 93%, is excellent. The specificity is a measure of the model's ability to correctly classify negative measurements, in this case, the model can successfully determine low concentrations of NT-proBNP. As can be seen in Fig. 5 above, very few low concentration measurements were classified inaccurately. This allows us to confidently classify low concentration samples and rule out the heart failure diagnosis. While this is extremely useful, in our future work, we will continue to improve the sensitivity to allow for better ruling in of heart failure.

## 4. Conclusion

NT-proBNP is a clinically important cardiovascular disease biomarker. A photonic crystal-enhanced fluorescence imaging immunoassay biosensor has been created for this analyte, capable of detecting clinically relevant levels of NT-proBNP. Photonic diatom frustules achieve fluorescence signal intensity enhancement of fluorophores as high as 2×compared with those on the flat glass substrate. Furthermore, using PLSR, a predictive model has been extracted and validated on a test dataset showing excellent linearity with a R<sup>2</sup> of 0.86 and a RMSEP of 14.47. This model can be applied to an unknown measurement and quantify the analyte concentration far surpassing the clinical detection requirement, with an excellent measurement accuracy. To prove the potential for clinical testing, the biosensor was employed to screen NT-proBNP in human plasma and we were able to successfully implement SVM classification with an excellent test specificity of 93% to rule out heart failure with further optimization being done to improve its ability to rule in heart failure. In short, we have successfully shown that diatom frustules can be used as fluorescence imaging immunoassay platform to detect NT-proBNP. The statistical regressions and classifications we have developed can be used for the

**Table 1**Binary classification results from NT-proBNP detection in plasma.

|            | Training                               |                                        |                                        | Testing                                |                                        |                                        |
|------------|----------------------------------------|----------------------------------------|----------------------------------------|----------------------------------------|----------------------------------------|----------------------------------------|
|            | Accuracy                               | Sensitivity                            | Specificity                            | Accuracy                               | Sensitivity                            | Specificity                            |
| SVM<br>kNN | $0.933 \pm 0.015$<br>$0.806 \pm 0.019$ | $0.870 \pm 0.030$<br>$0.813 \pm 0.044$ | $0.995 \pm 0.007$<br>$0.800 \pm 0.039$ | $0.775 \pm 0.034$<br>$0.605 \pm 0.054$ | $0.650 \pm 0.071$<br>$0.590 \pm 0.129$ | $0.930 \pm 0.045$<br>$0.620 \pm 0.144$ |

detection and classification of NT-proBNP levels. This easy-to-use and cost-effective immunoassay can achieve clinically relevant levels of detection while avoiding the complexity of current ECL method of detection.

#### Acknowledgements

The authors would like to acknowledge the support from the National Institutes of Health under Grant No. 1R21DA0437131, the National Science Foundation under Grant No. 1701329, and the support from Marine Polymer Technologies, Inc. The group would also like to thank Dr. Li-Jing Cheng for the use of his fluorescence microscope in these experiments.

## Appendix A. Supplementary data

Supplementary material related to this article can be found, in the online version, at doi:https://doi.org/10.1016/j.snb.2019.03.102.

#### References

- [1] D. Mozzafarian, E. Benjamin, A. Go, D. Arnett, M. Blaha, M. Cushman, S. Das, S. Ferranti, J. Despres, H. Fullerton, V. Howard, M. Huffman, C. Isasi, M. Jimenez, S. Judd, B. Kissela, J. Lichtman, L. Lisabeth, S. Liu, R. Mackey, D. Magid,
  - D. McGuire, E. Mohler, C. Mov, B. Muntner, M. Mussolino, K. Nasir, R. Neumar,
  - G. Nichol, L. Palaniappan, D. Pandey, M. Reeves, C. Rodriguez, W. Rosamond, P. Sorlie, J. Stein, A. Towfight, T. Turan, S. Virani, D. Woo, R. Yeh, M. Turner, Circulation 133 (2016) e38–e360.
- [2] P. Heidenreich, J. Trogdon, O. Khayjou, J. Butler, K. Dracup, M. Ezekowitz, E. Finkelstein, Y. Hong, S. Johnston, A. Khera, D. Loyd-Jones, S. Nelson, G. Nichols, D. Orenstein, P. Wilson, Y. Woo, Circulation 123 (2011) 933–944.
- [3] P. Ponikowski, A. Voors, S. Anker, H. Bueno, J. Cleland, A. Coats, V. Falk,
  - J. Gonzalez-Juanatey, V.-P. Harjola, E. Jankowska, M. Jessup, C. Linde,
  - P. Nihoyannopoulos, J. Parissis, B. Pieske, J. Riley, G. Rosano, L. Ruilope, F. Ruschitzka, F. Rutten, P. Meer, ESC Scientific Document Group, Eur. Heart J. 37 (2016) 2129–2200.
- [4] M. Weber, C. Hamm, Heart 92 (2006) 843–849.
- [5] J. Januzzi, C. Camargo, S. Anwaruddin, A. Baggish, A. Chen, D. Krauser, R. Tung, R. Cameron, J. Nagurney, C. Chae, D. Lloyed-Jones, D. Brown, S. Foran-Melanson, P. Sluss, E. Lee-Lewandrowski, K. Lewandrowski, Am. J. Cardiol. 95 (2005) 948–954.
- [6] Cobas, 20 Years of Innovation and Experience With Elecsys<sup>\*</sup>, 20 December (2017) www.cobas.com/home/product/clinical-and-immunochemistry-testing/ technology-elecsys-ecl.html.
- [7] Mayo Medical Laboratories, Test ID: PBNP NT-Pro B-Type Natriuretic Peptide (BNP), Serum. 20 December (2017) www.mayomedicallaboratories.com/test-catalog/Performance/84291.

- [8] J. Golden, F. Ligler, Biosens. Bioelectron. 9 (2002) 719-725.
- [9] B. Lee, S. Kim, Y. Ko, J. Park, S. Ji, M. Gu, Biosens. Bioelectron. 126 (2019) 122–128.
- [10] E. Song, M. Yu, Y. Wang, W. Hu, D. Cheng, M. Swihart, Y. Song, Biosens. Bioelectron. 72 (2015) 320–325.
- [11] X. Huang, S. Zhan, H. Xu, X. Meng, Y. Xiong, X. Chen, Nanoscale 8 (2016)
- [12] F. Liu, J. Choi, T. Seo, Biosens. Bioelectron. 25 (2010) 2361-2365.
- [13] A. Agrawal, C. Zhang, T. Byassee, R. Tripp, S. Nie, Anal. Chem. 78 (2006) 1061–1070.
- [14] L. Cai, N. Friedman, X. Xie, Nat. 440 (2006) 358-362.
- [15] J. Lee, H. Choi, J. Chang, J. Immunol. Methods 362 (2010) 38-42.
- [16] M. Wilkins, B. Turner, K. Rivera, S. Menegatti, M. Daniele, Sens. Biosensing Res. 21 (2018) 46–53.
- [17] A. Bek, R. Jansen, M. Ringler, S. Mayilo, T. Klar, J. Feldmann, Nano Lett. 8 (2007) 485–490.
- [18] M. Mohamed, V. Volkov, S. Link, M. El-Sayed, Chem. Phys. Lett. 317 (2000) 517–523.
- [19] A. Parfenov, I. Gryczynski, J. Malicka, C. Geddes, J. Lakowicz, J. Phys. Chem. B 107 (2003) 8829–8833.
- [20] S. Chakravarty, Y. Zou, W.-C. Lai, R. Chen, Biosens. Bioelectron. 38 (2012) 170-176
- [21] N. Ganesh, W. Zhang, P. Mathias, E. Chow, J. Soares, V. Malyarchuk, A. Smith, B. Cunningham, Nat. Nanotechnol. 2 (2007) 515–520.
- [22] J. Hou, H. Zhang, Q. Yang, M. Li, Y. Song, L. Jiang, Angew. Chem. 53 (2014) 5791–5795.
- [23] A. Pokhriyal, M. Lu, V. Chaudhery, C.-S. Huang, S. Schulz, B. Cunningham, Opt. Express 18 (2010) 24793–24808.
- [24] M. Campbell, D.N. Sharp, M.T. Harrison, R.G. Denning, A.J. Turberfield, Nat. 404 (2000) 53–56.
- [25] C.-C. Cheng, A. Scherer, J. Vac. Sci. Technol. 13 (1995) 2696-2700.
- [26] P.-E. Buffet, L. Poirier, A. Zalouk-Vergnoux, C. Lopes, J.-C. Amiard, P. Gaudin, C. Faverney, M. Guibbolini, D. Gilliland, H. Perrein-Ettajani, E. Valsami-Jones, C. Mouneyrac, Chemosphere 100 (2014) 63–70.
- [27] D. Larson, W. Zipfel, R. Williams, S. Clark, M. Bruchez, F. Wise, W. Webb, Sci. 300 (2003) 1434–1436.
- [28] R. Diez, M. Ortiz, L. Sarabia, I. Birlouez-Aragon, Anal. Chim. Acta 606 (2008) 151–158.
- [29] O. Divya, A. Mishra, Talanta 72 (2006) 43-48.
- [30] X. Yan, H. Li, X. Han, X. Su, Biosens. Bioelectron. 74 (2015) 277-283.
- [31] C. Kurachi, C. Fontana, L. Rosa, V. Bagnato, J. Biomed. Opt. 13 (2008) 034018.
- [32] D. Moshou, X.-E. Pantazi, D. Kateris, I. Gravalos, Biosys. Eng. 117 (2014) 15–22.
- [33] Y. Zhang, X. Zhou, R. Witt, B. Sabatini, D. Adjeroh, S. Wong, Neruoimage 36 (2007) 346–360.
- [34] X. Kong, K. Squire, E. Li, P. LeDuff, G. Rorrer, S. Tang, B. Chen, C. McKay, R. Navarro-Gonzalez, A. Wang, IEEE Trans. Nanobiosci. 15 (2016) 828–834.
- [35] X. Kong, Y. Xi, P. Le Duff, X. Chong, E. Li, F. Ren, G.L. Rorrer, A.X. Wang, Biosens. Bioelectron, 88 (2017) 63–70
- [36] F. Ren, J. Campbell, X. Wang, G. Rorrer, A. Wang, Opt. Express 21 (2013) 15308–15313.
- [37] K. Squire, X. Kong, P. LeDuff, G. Rorrer, A. Wang, J. Biophotonics 11 (2018) e201800009.
- [38] C.-C. Chang, C.-J. Lin, ACM Trans. Intell. Syst. Technol. 2 (2011) 1–27.